# Particle modeling of radial electron dynamics in a controlled discharge of a Hall thruster

A. Domínguez-Vázquez[1], F. Taccogna[2], E. Ahedo[1]
[1]Universidad Carlos III de Madrid, 28911 Leganés, Spain
[2]CNR-NANOTEC - PLasMI Lab, via Amendola 122/D, 70126 Bari, Italy
March 21, 2018

**Abstract**

An improved radial particle-in-cell model of an annular Hall effect thruster discharge with secondary-electron emission from the walls and a radial magnetic field is presented. New algorithms are implemented: first, to adjust the mean neutral density to a desired mean plasma density; second, to avoid refreshing of axially accelerated particles; and third, to weigh correctly low density populations (such as secondary electrons). High-energy tails of the velocity distribution functions of primary electrons and secondary electrons from each wall are largely depleted, leading to temperature anisotropies for each species. Secondary electron populations are found to be partially recollected partially thermalized into the primary population. A replenishment ratio of the primary high-energy tail is determined based on the sheath potential fall. Significant asymmetries at inner and outer walls are found for the collected currents, the mean impact energy, the wall and sheath potentials, the two beams of secondary electrons. Radial profiles in the plasma bulk are asymmetric too, due to a combination of the geometric expansion, the magnetic mirror effect, and the centrifugal force (emanating from the $E \times B$ drift). Temperature anisotropy and non-uniformity, and the centrifugal force modify the classical Boltzmann-Maxwell relation on electrons along the magnetic lines.

## 1 Introduction

The Hall effect thruster (HET) [1–3] is a mature technology, already widely and successfully used as both primary and secondary propulsion system for a variety of space missions. In spite of its success, relevant physical phenomena of the plasma discharge inside the HET chamber and in its near plume are insufficiently known. This shortage drags out the development of new designs for new applications (for instance at low or high powers) and optimization of existing ones. Also, it blocks the development of reliable and predictive simulation tools, which are considered essential, not only for design purposes, but also for accelerating tests of lifetime and of operation at different conditions (e.g. high thrust and high specific impulse).

One of the main open problems is the effects of the plasma interaction with the walls of the thruster chamber on the electron velocity distribution function (VDF) and the subsequent energy losses and plasma recombination there. Due to the electric potential structure, electrons are a confined population except for the small currents that flow to the walls or downstream forming the plasma jet. This confinement would facilitate the electron thermalization, but the low collisionality of the discharge (at plasma densities of $10^{17}$-$10^{18}\mathrm{m}^{-3}$) makes that the VDF tails of electrons collected by the walls are not fully replenished, and hence the VDF is non-Maxwellian. A second issue, particularly acute for the ceramics used in HET chambers, is the large secondary electron emission (SEE) caused by impact of 'primary' electrons from the plasma bulk. This generates counterstreaming flows of secondary electrons [4–6] making further non-Maxwellian the VDF.

Ahedo and Parra [7] considered a one-dimensional planar (1Dp) stationary fluid model to analyze the plausible case where the SEE was partially trapped within the plasma bulk (and eventually thermalized) and partially recollected by the walls; they determined the effects of partial recollection on the potential fall in the sheaths (and its charge saturation) and on the energy flows to the walls. Later, Ahedo and dePablo [8] extended the analysis to partial thermalization of both primary and secondary electrons with a 1Dp stationary kinetic model, describing the non-Maxwellian VDF and the SEE yields with phenomenological parameters; they obtained analytical expressions for the sheath potential fall and the energy losses to the walls, in terms of the model parameters.

Sydorenko, Kaganovich, and coworkers [9,10] treated a similar time-dependent 1Dp problem with a Particle-in-cell(PIC)/Monte-Carlo-Collision(MCC) formulation [11, 12]. Using a fixed background of neutrals, their steady-state solution confirmed the partial recollection of SEE at the walls and, more importantly, determined the temperature anisotropy ratio of the VDF, in terms of the axial electric field, collisional frequencies, and SEE yields; interestingly, the near-wall conductivity effect [13] in the axial electron current was observed too. More recently, Wang et al. [14] investigated, with a similar 1Dp PIC/MCC model, the asymmetries in the electric potential profile and sheath potential falls caused by having different SEE yields at each wall (i.e. different materials).

Taccogna et al. [15–17] considered a 1D-radial (1Dr) PIC/MCC model, much more suitable to simulate a HET annular chamber and where the asymmetry on the electric potential profile takes place naturally. The emphasis

of these works is on the development of a strong asymmetry and a saturated stream instability propagating all along the radial domain, in conditions where a large axial electric field induces an azimuthal electron drift of the order of the electron thermal speed.

This paper revisits the model and code of Taccogna with two types of goals. The first one is to enrich the numerical consistency and capabilities of the code and, at the same time, to analyze the intrinsic limitations of 1Dp and 1Dr models. To this respect and even assuming azimuthal symmetry (i.e. $\partial/\partial\theta = 0$) the reduction of an axilsymmetric $(r, z)$ discharge to a given axial section of the chamber implies that strong assumptions must be made on all terms related to the axial plasma flows and forces. As a consequence, there is a certain degree on arbitrariness on the 1D results, that cannot be let aside when drawing conclusions. The second goal of the paper is to investigate further the steady-state solution (without stream instabilities) with the focus on assessing the temperature anisotropy ratio of the VDF of both primary and secondary electrons, combined with the asymmetries introduced by the cylindrical geometry (which includes geometrical expansion, centrifugal forces, and magnetic mirror effects). Finally, the influence of anisotropy and asymmetry in macroscopic laws of interest is investigated.

The rest of the paper is organized as follows. The main physical aspects of the model are presented in Sec. 2, while Sec. 3 includes the numerical implementation and the validation of the new algorithms. A discussion of the main physical aspects of the plasma discharge is provided in Sec. 4. Conclusions are drawn on Sec. 5.

# 2 The 1D radial model

The model attempts to analyze the plasma radial structure at a given axial location within the acceleration region of a HET chamber, taking into consideration the weak plasma collisionality and the SEE emission from the walls due to impacts of energetic primary electrons. Figure 1 sketches the annular HET chamber with $r_1$ and $r_2$ as inner and outer radius, respectively; $A = \pi(r_2^2 - r_1^2)$ is the area of the section and, when convenient, magnitudes are expressed per unit of axial length.

The 1Dr model considers electrons $e$, (singly-charged) ions $i$, and neutrals $n$. Neutrals are modeled just as a spatially-uniform population with a time-dependent density $n_n(t)$ and a constant temperature $T_n$. Electrons and ions are modelled as two populations of macroparticles with densities and temperatures, $n_j$ and $T_j$ $(j = i, e)$, evolving with $(r, t)$. Let be $\bar{n}_e(t)$ the radially-averaged electron density and take it as representative of the instantaneous plasma density.

We are interested in simulating a quasi-stationary discharge with a certain mean plasma density, that is $\bar{n}_e(t) \approx \bar{n}_e(0) \equiv n_{e0}$. In a 1D model, this requires to take some decisions on the behavior of the particle sources and sinks. In a cylindrical geometry, the conservation equations for ions and electrons reduce to

$$\frac{\partial n_j}{\partial t} + \frac{1}{r}\frac{\partial}{\partial r}(r n_j u_{rj}) = S_{ioniz} + S_{axial,j}, \qquad j = i, e, \tag{1}$$

where: $n_j u_{rj}$ is the species radial flux; $S_{ioniz}$ is the source term due to ionization, proportional to $n_n(t)$; and $S_{axial,j}$ is the source term due to the net axial contribution for species $j$. In a 2D $(r, z)$ model one would have $S_{axial,j} = \partial(n_j u_{zj})/\partial z$, but, here $S_{axial,j}$ is as arbitrary as the HET axial section we are attempting to simulate. In quasi steady-state, the integral of the continuity equation over the plasma volume (expressed in electric current units) yields

$$I_{wall,j} \approx I_{ioniz} + I_{axial,j}, \qquad j = i, e, \tag{2}$$

with $I_{wall,j}$ the species current lost into the wall, $I_{ioniz}$ the (equivalent) current created through volumetric ionization (the same for electrons and singly-charged ions and proportional to $n_n$), and $I_{axial,j}$ the current injected (or extracted) through the axial flow. While $I_{wall,j}(t)$ is obtained directly from the dynamic plasma response, both $I_{ioniz}$ and $I_{axial,j}$ depend on the particular model formulation.

If $n_n(t)$ is known, then plasma variables determine completely $I_{ioniz}(t)$, and to simulate a stationary discharge requires $I_{axial,j} \approx I_{wall,j} - I_{ioniz}$. This implies a continuous injection (or extraction) of plasma from the domain, requiring to define properties on the injected macroparticles or selection criteria for the extracted ones. We can distinguish between *axially-controlled* and *ionization-controlled* discharges depending on whether $I_{axial,j}$ is much larger or much smaller than $I_{ioniz}$, respectively. In an axially-controlled discharge, the plasma response is largely set by these conditions 'external' to the radial dynamics. Previous works seem to use $n_n(t) = n_{n0}$ and thus would operate in a mixed regime.

The present work implements a model for fully ionization-controlled discharge with $S_{axial,i} = S_{axial,e} = 0$ and $n_n(t)$ being adjusted in order that

$$I_{ioniz}(t) \approx I_{wall,j}(t), \tag{3}$$

at any time (with some tolerance). It will be shown that adjusting $n_n(t)$ is simple and it assures that a stationary discharge is achieved. Besides, it corresponds reasonably to the physical situation in the channel acceleration region, where ionization and wall recombination were found to compensate each other [6].

A 1Dr model needs also to prescribe the axial electric field $E_z$. This field accelerates over time the (nearly-unmagnetized) ions, which is an undesirable secular effect on the simulation. Previous works have dealt with this issue by resetting or refreshing occasionally the ion population. Here, it is chosen to just ignore the effect of $E_z$ on the ions, which can be interpreted as a continuous axial refreshing of ions. Therefore, macro-ions are inserted initially or created later with a mean axial velocity $u_{zi}$, and they are advanced only with the radial electric field (and the magnetic field). Thus $E_z$ affects electrons only, primarily by forcing with the magnetic field the electron $E \times B$ azimuthal drift. In fact, a key validation of the model will be to check that there is not a secular increase of the macroscopic axial velocities of ions and electrons.

While $E_z$ is taken constant and known, the radial electric field, $E_r = -d\phi/dr$, with $\phi(r,t)$ the electric potential, satisfies the Poisson equation

$$\frac{\varepsilon_0}{r}\frac{\partial}{\partial r}\left(r\frac{\partial \phi}{\partial r}\right) = \rho_{el}(r,t), \tag{4}$$

with $\rho_{el}$ the net electric charge of the plasma. The two boundary conditions required to integrate this equation are set, for instance, at the outer wall, $r = r_2$,

$$\phi_2 = 0 \qquad \varepsilon_0 E_{r2} = -\sigma_2(t) \tag{5}$$

where the first condition just sets a reference for the potential, $\varepsilon_0$ is the vacuum permittivity, and $\sigma_2$ is the surface charge at the outer dielectric wall, to be defined in detail below. A similar relation on $E_r$ at $r = r_1$ is derived below in Eq.(9).

The magnetic field is assumed radial and, in order to be divergent-free, it satisfies

$$B_r(r) = B_{r_1}\frac{r_1}{r}, \tag{6}$$

with $B_{r1}$ known. Since $B_{r_2}/B_{r_1} = r_1/r_2 = 0.7$, a noticeable mirror effect on electrons could be possible.

Turning now to plasma-wall interaction, ions and electron reaching the radial walls are collected (formally); ion recombination is not considered explicitly since neutrals are modeled through $n_n(t)$. SEE produced by the impacting electrons will follow the probabilistic model of Ref. 18. In this model, the total SEE yield accounts for three different types of secondary electrons: backscattered ones (elastically reflected by the wall), re-diffused ones (non-elastically reflected by the wall) and the so called true secondary electrons (those extracted from the surface layers of the material). More details on the implementation of the SEE model is given in [16]. For the present purpose of understanding better the radial discharge and electron distribution function, backscattered and rediffused electrons are being switched off, so that SEE is limited to true secondary (TS) electrons. In the energy range of interest, the true-secondary-only electron emission yield (i.e true-secondary-to-primary flux ratio) reduces to

$$\delta_{TS}(E) \simeq E/E_c \tag{7}$$

with $E$ the impact electron energy, and $E_c$ the crossover energy ($E_c = 51.1$eV in simulations here). After emission from the wall, true secondary electrons take first a preferential radial motion due to their rapid acceleration by the large $E_r$ ($\sim 500$V/cm) within the Debye sheath. Then, they become magnetized, acquiring the azimuthal drift and the gyromotion. Dispersion velocity of this population is due to occasional collisions.

The surface charges at each of the two material walls are created by accumulation over time of the net radial electric current to the wall

$$\sigma_l(t) = -\int dt \boldsymbol{j}_l(t)\cdot \mathbf{1}_l, \quad l = 1,2, \tag{8}$$

where $\boldsymbol{j}_l$ is the electric current density and $\mathbf{1}_l$ is the wall normal pointing towards the plasma. Integration of the Poisson equation across each of the wall surfaces yields

$$\varepsilon_0 E_{r2} = -\sigma_2(t), \qquad \varepsilon_0 E_{r1} = \sigma_1(t). \tag{9}$$

The first condition was already imposed as boundary condition in Eq. (5). Consistency requires that the second one is not an independent condition, that is be satisfied automatically. This is indeed the case since the radial integration of the electric charge conservation and Poisson equations yield

$$\varepsilon_0[rE_r]_{r_1}^{r_2} = -\int [rj_r]_{r_1}^{r_2} dt. \tag{10}$$

The collisional processes included in the code are the following. First, there are electron-neutral collisions including elastic scattering, excitation and single ionization, following the models of Refs. 19–21 and using for neutrals, $n_n(t)$ and $T_n$. Second, electron-ion, electron-electron and ion-ion Coulomb collisions, according to the

models of Refs. 22–25. Ion-neutral collisions are found to be negligible for typical HET parameters. Secondary (i.e. wall born) electrons are transferred to the main primary population (i.e. they 'thermalize') when they undergo a collision with neutrals or a large angle (higher than 90 degrees) Coulomb collision. Notice that, in a kinetic or particle formulation, this distinction between 'secondary' and 'primary' populations is just convenient for the analysis of the plasma response. On the contrary, that distinction acquires full sense in multi-fluid electron models.

# 3 Numerical implementation and validation

The main model input parameters and resulting plasma magnitudes are listed on Table 1. The simulation is carried out per unit of axial length, that is the simulation volume is equal to the axial section area $A$. A uniform radial mesh of $N_r + 1$ points from $r_1$ to $r_2$ is chosen, with a cell size $\Delta r$ smaller than the plasma Debye length $\lambda_D$. Electron and ion macro-particles have the same constant weight $W$ throughout the simulation, chosen so that the initial number of both electron and ion macro-particles is $N_{p0} \approx 10^5$, corresponding to about 70 macro-particles per cell. It has been checked that using the double number of particles per cell reduces only the PIC fluctuations, without changing the averaged trends.

Xenon is assumed as propellant. Plasma macroscopic properties such as particle densities and fluxes are computed at the mesh nodes through an area weighting algorithm [26]. The nodal weighting volumes are corrected according to Ref. 27. Higher moments of the distribution function such as the temperature are obtained for each simulated species through a new extended volumetric weighting (EVW) approach presented in Sec. 3.2. Additionally, surface weighting schemes [28, 29] are used for updating the particle fluxes to the walls.

In order to obtain the electric potential at the mesh nodes, second order finite difference schemes are used for discretizing Poisson equation along the cylindrical radial coordinate $r$. The Thomas tridiagonal algorithm [30] is applied as direct solving technique. The electrons trajectories are propagated along time using both radial and axial components of the electric field, and the radial magnetic field. In contrast, only the radial electric field is used to update the ions' velocity and position. The Boris-Buneman leapfrog algorithm [26] is applied to move all macro-particles one time step forward considering the corresponding electric and magnetic fields interpolated to the macroparticles position. The time step is chosen so that $\Delta t < 0.3\omega_{pe}^{-1}$, where $\omega_{pe}$ is the plasma frequency. This condition ensures an accurate integration of the electron gyromotion since $\omega_{pe} > \omega_{ce}$, with $\omega_{ce}$ the electron gyrofrequency (see Table 1).

After advancing all macro-particles every time step, a MCC module is called to perform electron-neutral collisions including elastic scattering, excitation, and single ionization. As aforementioned, the neutral gas is simulated as a spatially uniform background with constant temperature $T_n$ and density $n_n(t)$. The constant time step method of Refs. [19, 20] for selecting the type of collision is implemented using the cross sections from Ref. 31. The probability distribution function for the progeny electrons generated by ionization is taken from [21]. A mean axial velocity $u_{zi}$ is added to any new-born ion. Regarding the emission of true-secondary electrons, a zero-drift semi-Maxwellian distribution with temperature $T_{eW} = 2\text{eV}$ is assumed.

In general, new simulations are initiated assuming uniform Maxwellian populations of electrons and ions of the same density and a radially constant potential. In the first timesteps, this implies large electron currents to the walls. These build surface charges there, that create the Debye sheaths confining electrons. The surface charges stabilize when the net electric currents to the walls becomes zero, Eq. (8).

## 3.1 The discharge control algorithm

An algorithm for an ionization-controlled discharge with no axial contributions of plasma is presented here. In principle, there would be two methods to proceed, both plotted in Fig. 2(a). The first one, used in previous works and represented by the dashed lines, fixes the neutral density, i.e. $n_n(t) = n_{n0}$ and let $\bar{n}_e(t)$ to evolve until s final state is reached after a few microseconds (a time related to the transit time of ions). The second method, represented by the solid lines of Fig. 2(a) and Fig. 2(b) fixes the mean plasma density in the domain, $\bar{n}_e(t) \simeq \bar{n}_{e0}$, and adjusts $n_n(t)$ in order to satisfy Eq. (3).

In the first method the final plasma density is unknown and it can be very different from the initial one. For instance, the case $n_n(t) = 4 \cdot 10^{18}\text{m}^{-3}$ starts with $\bar{n}_e \approx 8 \cdot 10^{16}\text{m}^{-3}$ and ends, after 25 $\mu$s, with $\bar{n}_e \approx 6 \cdot 10^{15}\text{m}^{-3}$, This implies that starting with 80 macro-electrons per cell, we end with only 6 macro-electrons per cell, and thus much worse weighted magnitudes. The advantage of the novel second method is that the number of macro-particles does not change practically along the simulation and thus can be optimized. Besides, it seems more preferable to fix from the beginning the mean plasma density we are targeting to, than the neutral density.

The second method is here implemented with the following ionization-controlled discharge (ICD) algorithm

| Type | Description | Symbol | Units | Value |
|---|---|---|---|---|
| **Populations settings** | Number of elementary particles per macro-particle | $W$ | - | $3 \cdot 10^9$ |
| | Initial average plasma density | $n_{e0}$ | $10^{17}\mathrm{m}^{-3}$ | 0.8 |
| | Initial number of ions and electrons* | $N_{p0}$ | - | 106814 |
| | Initial electron temperature | $T_{e0}$ | eV | 10 |
| | Initial ion temperature | $T_{i0}$ | eV | 1 |
| | Ion axial mean velocity | $u_{zi0}$ | km/s | 10 |
| | Initial background neutral density | $n_{n0}$ | $10^{17}$ $\mathrm{m}^{-3}$ | 40 |
| | Neutral temperature | $T_{n0}$ | K | 700 |
| **E, B fields** | Electric field axial component | $E_z$ | V/cm | 100 |
| | Magnetic field radial component at inner radius | $B_{r_1}$ | G | 150 |
| **Simulation parameters** | Inner radius | $r_1$ | cm | 3.5 |
| | Outer radius | $r_2$ | cm | 5.0 |
| | Number of nodes | $N_r$ | - | 1500 |
| | Grid spacing* | $\Delta r$ | $\mu$m | 10 |
| | Time step | $\Delta t$ | ps | 5 |
| **Physical parameters** | Debye length* | $\lambda_D$ | $\mu$m | 83.1 |
| | Electron Larmor radius* | $r_l$ | $\mu$m | 802.0 |
| | Inverse of plasma frequency* | $1/\omega_{pe}$ | ps | 62.7 |
| | Inverse of electron cyclotron frequency* | $1/\omega_{ce}$ | ps | 379.1 |

Table 1: Main input parameters including initial population settings, externally applied fields and grid definition. The magnitudes marked with an asterisk (*) are not input parameters of the model, but are derived from the other parameters instead. The variables named as physical parameters are estimated from the other input values given at initial conditions.

on neutrals. First, a tolerance is fixed for the variations of average plasma density,

$$\epsilon_{c1} = |\bar{n}_e(t)/\bar{n}_{e0} - 1| \tag{11}$$

($\epsilon_{c1} = 10^{-3}$ in the simulations here). Then, every PIC-MCC time step, both $\bar{n}_e(t)$ and its rate of change are computed, the last one defined as

$$\Delta\bar{n}_e^{(k)} = \frac{1}{k_c}\left[n_e^{(k)} - n_e^{(k-1)} + (k_c - 1)\Delta\bar{n}_e^{(k-1)}\right] \tag{12}$$

where $(k-1)$ and $(k)$ are two subsequent instants of PIC-time and $k_c$ is a fixed number of time steps ($k_c = 100$ in the figures here).

The neutral density for instant $(k+1)$ is modified only if $|\bar{n}_e(t)/\bar{n}_{e0} - 1|$ is outside the above tolerance range, and

$$|\Delta\bar{n}_e^{(k)}| > \epsilon_{c2} \tag{13}$$

with $\epsilon_{c2}$ fixed ($10^{-2}$ in the figures here). The reason to include a condition on the time-extended rate of change, $\Delta\bar{n}_e$ is to filter the fast oscillations and numerical noise inherent to the PIC calculations. The updated neutral density is defined as

$$n_n^{(k+1)} = n_n^{(k)} \frac{\bar{n}_{e0}}{\bar{n}_e^{(k)}}. \tag{14}$$

Figure 2(b) shows that the stationary discharge with $\bar{n}_e \simeq 8 \cdot 10^{16}\mathrm{m}^{-3}$ requires $n_n \approx 6.85 \cdot 10^{18}\mathrm{m}^{-3}$.

The ICD algorithm is not applied until the surface charges $\sigma_j$ are practically stabilized after the formation of the Debye sheaths. Figures 2(c) and 2(d) show the evolution of the surface charges and the potential at the central point $M$, i.e. $r_M = 42.5$mm. Figure 2(d) also plots the evolution for non-ICD, with $n_n(t) = n_{n0}$. Observe that it takes about $1\mu$s ($\sim 2 \cdot 10^5$ PIC timesteps) to establish the Debye sheaths.

Figures 2(e) and 2(f) detail the time evolution of partial currents for an ICD and a non-ICD case, respectively. The net electric current to the two walls is there split in three populations: ions impacting the two walls ($I_{wi}$), electrons going *to* and impacting the walls ($I_{wet}$), and (true-secondary) electrons emitted *from* the walls ($I_{wef}$). The ICD case satisfies very well the steady-state and dielectric conditions,

$$I_{ioniz} = I_{wi} = I_{we}, \qquad I_{we} \equiv I_{wet} - I_{wef}, \tag{15}$$

thus validating the ICD algorithm. On the contrary, the non-ICD, satisfies well the dielectric condition but, there is a deficit in ionization. As a consequence, the mean plasma density decreases [see Fig. 2(a)] and (with the ion transit delay) the currents to the walls too, until the discharge seems to extinguish.

### 3.2 The extended volumetric weighting algorithm

The PIC formulation operates with a constant macro-particle weight $W$ for all the simulated species, which simplifies the treatment of collisional processes and saves computer memory. However, it also implies that, for each species, the number of macroparticles per cell is proportional to its density. The simulation parameters are optimized to reproduce well the response of the main species, ions and primary electrons, with similar densities (except inside the sheaths). But secondary electrons from the walls turn out to have a density 1-2 orders of magnitudes lower. Thus, if there are 50-100 particles per cell for ions and primary electrons, there will be only 1-10 for secondary electrons. This leads to temporal oscillations on their density and, more importantly, to wrong estimates of their macroscopic velocity and temperature, as it will be shown below.

This issue can be solved by extending in time the conventional volumetric weighting of particles. The extended volumetric weighting algorithm (EVW) proposed here takes into consideration data from the last $N_k$ timesteps. The particle density of species $j$ in a given node satisfies

$$n_j = \frac{W}{N_k \Delta V} \sum_k \sum_p s_p, \tag{16}$$

where $\Delta V$ is the weighting volume associated to the node, $s_p$ is the linear weighting function assigning a weight to each macroparticle depending on its relative position and distance to the node, the sum in $p$ is for all macroparticles with $s_p \neq 0$, and the sum in $k$ is for the timesteps. Similarly, the particle flux vector at the same node and time is given by

$$\boldsymbol{g_j} = \frac{W}{N_k \Delta V} \sum_k \sum_p \boldsymbol{v}_p s_p, \tag{17}$$

with $\boldsymbol{v}_p$ the particle velocity. Then, the resultant fluid velocity is $\boldsymbol{u_j} = \boldsymbol{g_j}/n_j$.

In the same way, the diagonal components of the pressure tensor at the same node and instant are computed as

$$p_{lj} = \frac{m_e W}{N_k \Delta V} \sum_k \sum_p (v_{lp} - u_{lj})^2 s_p, \qquad l = r, \theta, z, \tag{18}$$

and the resultant temperatures are $T_{lj} = p_{lj}/n_j$.

Of course,the EVW is filtering oscillations of frequencies $(N_k \Delta t)^{-1}$ but this is not an issue when studying the steady-state discharge. For instance, in the simulations shown in this paper, values of $N_k = 10^4 - 10^5$ are taken, which correspond to 0.05-0.5$\mu$s, so even simulations of up to hundreds of kHz can be reproduced correctly.

Figure 3 plots the azimuthal velocity and the mean temperature of the three electron species considered hereafter: primary electrons $p$, and secondary electrons emitted by the inner $s1$ and outer $s2$ walls (remind that secondary electrons become primary electrons after a large angle collision). In order to show the need and the good performance of the EVW algorithm, these two macroscopic variables are plotted in two ways. The plotted EVW variables correspond to

$$\boldsymbol{u}_e = \frac{\sum_k \sum_p \boldsymbol{v}_p s_p}{\sum_k \sum_p s_p}, \qquad T_e = \frac{m_e}{3} \frac{\sum_k \sum_p |\boldsymbol{v}_p - \boldsymbol{u}_e|^2 s_p}{\sum_k \sum_p s_p}. \tag{19}$$

The conventional volumetric weighting variables (averaged over $N_k$ timesteps, to make fairer the comparison) correspond to

$$\boldsymbol{u}'_e = \frac{1}{N_k} \sum_k \frac{\sum_p \boldsymbol{v}_p s_p}{\sum_p s_p}, \qquad T'_e = \frac{m_e}{3N_k} \sum_k \frac{\sum_p |\boldsymbol{v}_p - \boldsymbol{u}'_e|^2 s_p}{\sum_p s_p}. \tag{20}$$

The vertical dashed lines in Fig. 3 represent approximately the edges of the Debye sheaths, here located at 0.5mm from the wall and where the radial ion Mach number is approximately 1 [see Fig. 5(c) below]. The definition of 'sheath edges' in the present one-scale model is just meant for discussion purposes, since plasma response is known to change sharply when entering the thin Debye sheaths.

In Fig. 3(a) we observe that applying the EVW, the azimuthal velocities of the three electron populations satisfy the $E \times B$ drift. This result is particularly important to validate the simulation of the dynamics of secondary electrons: these are born with a very small azimuthal velocity but, after crossing the sheath, they must acquire the gyromotion and the $E \times B$ drift in a distance of about a gyrodiameter, i.e. about 1.6 mm. It is this physical argument that suggests that the conventional weighting yields incorrect (lower) values of $u_{\theta e}$ for secondary electrons. The reason would be that instantaneous values used in Eq. (20) are weighted over a too small number of macroparticles. The conventional weighting behaves well on $u_{\theta e}$ for primary electrons since enough number of macroparticles per cell are used at any timestep. For primary electrons, only within

the sheaths we observe some discrepancy between the two weightings, due precisely to the decreasing density (and thus number of macroparticles per cell) there.

The differences between the extended and the conventional weightings are more pronounced when computing temperatures, since these variables measure velocity dispersions, so the double summation on particles-per-cell (one for $\mathbf{u_j}$ an done for $T_j$ doubles the source of errors. In Fig. 3(b), the conventional weighting works fine for the primary electron temperature but it again underestimates much the temperatures of secondary electrons. Observe that it is practically zero for $s1$ electrons (a zero temperature is the natural value when there is only one particle per cell).

# 4 Analysis of electron distribution function and dynamics

The analysis here is focused on the stationary response for an ionization-controlled discharge defined in Table 1. Table 2 compiles relevant data of the discharge that will be commented along this section together with Figs. 4 to 6.

| Type and units | Description | Symbol | Value |
|---|---|---|---|
| **Electric potentials** (V) | At the mid radius $M$ | $\phi_M$ | 17.47 |
| | At the inner sheath edge $Q_1$ | $\phi_{Q_1}$ | 13.70 |
| | At the outer sheath edge $Q_2$ | $\phi_{Q_2}$ | 12.74 |
| | At the inner wall $W_1$ | $\phi_{W_1}$ | 2.27 |
| | At the outer wall $W_2$ | $\phi_{W_2}$ | 0.0 |
| **Collision frequencies** (MHz) | e-n elastic collision | $\nu_{en}^{el}$ | 3.680 |
| | e-n excitation collision | $\nu_{en}^{ex}$ | 0.209 |
| | e-n excitation collision | $\nu_{en}^{ion}$ | 0.168 |
| | e-i Coulomb collision | $\nu_{ei}^{Coul}$ | 0.076 |
| | e-e Coulomb collision | $\nu_{ee}^{Coul}$ | 0.017 |
| | i-i Coulomb collision | $\nu_{ii}^{Coul}$ | 0.119 |
| **Thermalization and wall collection fractions** (%) | $s1$ thermalization | - | 63.2 |
| | $s1$ collection at the inner wall | - | 7.5 |
| | $s1$ collection at the outer wall | - | 29.3 |
| | $s2$ thermalization | - | 60.1 |
| | $s2$ collection at the inner wall | - | 28.7 |
| | $s2$ collection at the outer wall | - | 11.2 |
| **Current densities** ($A/m^2$) | $p$ to the inner wall | $\lvert j_{p,1-}\rvert$ | 12.80 |
| | $s1$ to the inner wall | $\lvert j_{s1,1-}\rvert$ | 0.17 |
| | $s1$ from the inner wall | $\lvert j_{s1,1+}\rvert$ | 2.36 |
| | $s2$ to the inner wall | $\lvert j_{s2,1-}\rvert$ | 2.96 |
| | $p$ to the outer wall | $\lvert j_{p,2+}\rvert$ | 23.97 |
| | $s1$ to the outer wall | $\lvert j_{s1,2+}\rvert$ | 0.48 |
| | $s2$ to the outer wall | $\lvert j_{s2,2+}\rvert$ | 0.81 |
| | $s2$ from the outer wall | $\lvert j_{s2,2-}\rvert$ | 7.23 |
| **Mean impact energies per elementary particle** (eV) | $e \equiv p + s1 + s2$ at the inner wall | $E_{we,1}$ | 8.10 |
| | $p$ at the inner wall | $E_{wp,1}$ | 8.50 |
| | $s1$ at the inner wall | $E_{ws1,1}$ | 4.06 |
| | $s2$ at the inner wall | $E_{ws2,1}$ | 6.59 |
| | $e \equiv p + s1 + s2$ at the outer wall | $E_{e,2}$ | 15.75 |
| | $p$ at the outer wall | $E_{wp,2}$ | 16.16 |
| | $s1$ at the outer wall | $E_{ws1,2}$ | 6.24 |
| | $s2$ at the outer wall | $E_{ws2,2}$ | 9.34 |
| **Electron energy balance source and sink terms** (W) | Electric field work | $P_{elec}$ | 337.67 |
| | SEE energy gain | $P_{wall,f}$ | 5.56 |
| | Wall losses | $P_{wall,t}$ | 153.40 |
| | Inelastic collisions losses | $P_{inel}$ | 194.30 |

Table 2: Main parameters characterizing the steady-state discharge. Values averaged over the last micro-second of simulation have been used.

Figure 4(a) plots the radial profile of the self-adjusted electric potential. Again vertical dashed lines correspond to the sheaths edges. Points $W_1$, $W_2$, $Q_1$, $Q_2$, and $M$ correspond to walls, sheath edges, and channel mid radius, respectively. The maximum potential is located just a bit inwards of point $M$ and is only 0.03V higher. The asymmetry of the potential profile due to the different cylindrical effects is evident at sheath edges and walls. The potential difference between the two sheath edges is $\Delta\phi_{Q_1Q_2} = 0.96$V and between the two walls is $\Delta\phi_{W_1W_2} = 2.27$V. This last one is a bit higher than the typical emission energy of secondary electrons in our simulations, $T_{eW} = 2$eV. Thus, $\Delta\phi_{W_1W_2} > 0$ facilitates that electrons emitted from the wall $W_2$ be recollected at the wall $W_1$. However, there are two magnetic effects that change the perpendicular energy of an electron and therefore their radial energy and radial turning points (i.e. those with $v_r = 0$).

Neglecting collisions, the kinetic energy of an electron of total energy $E$ satisfies

$$E = m_e \frac{v_r^2 + v_\perp^2}{2} - e\phi. \tag{21}$$

In the small gyromotion limit, the phase-averaged perpendicular energy, $m_e v_\perp^2/2$ is the sum of the one due to the gyromotion (which is proportional to the conserved magnetic moment $\mu$) and the one due to the azimuthal $E \times B$ drift. Thus, here the radial kinetic energy satisfies

$$m_e \frac{v_r^2}{2} \simeq E + e\phi - \mu B - W_d = E + e\phi(r) - \mu B_1 \frac{r_1}{r} - W_{d1} \frac{r^2}{r_1^2}, \tag{22}$$

where $W_d = m_e E_z^2/2B_r^2$ is the gyrocenter azimuthal energy, and the right-most side makes explicit the variation of $B$ and $W_d$ with $r$; in our simulations $W_{d1} = 1.27$eV and $W_{d2} = 2.58$eV at inner and outer walls, respectively. Therefore, the radial energy of an electron moving inwards is decreased by the magnetic mirror and is increased by the change on the $E \times B$ drift. For the plotted simulation, the change on $W_d$ is mild, but non negligible, compared to the change of $\phi$ in the plasma bulk. Below it will be seen that this azimuthal energy remains as part of the electron macroscopic energy/momentum balance.

Figures 4(b)-(d) show the distribution functions $f_r(v_r)$ (once integrated over $v_\theta$ and $v_z$) of primary and secondary electrons, $p$, $s1$ and $s2$, at points $M$, $Q_1$ and $Q_2$. Observe first that, in the plasma bulk, between $Q_1$ and $Q_2$, the densities of secondary electrons are much lower than the density of primary electrons, so $n_p$ is going to determine almost exclusively the electric potential profile. In each subfigure (b)-(d), the solid vertical lines separate approximately (and in the absence of collisions) the central region of confined electrons from the left and right regions or electrons to be collected by the inner and outer wall, respectively. These lines correspond to the radial turning points from Eq. (22) for electrons with an average value of the gyroenergy $< \mu B >= 9.2$ eV.

Table 2 shows that Coulomb collisions are negligible compared to collisions with neutrals, but even the elastic electron-neutral frequency, $\sim 3.7$ MHz, is low compared with the transit frequency, $\sim 62$MHz. This explains that the VDFs at point $M$, Fig. 4(b), present a large depletion of the high-energy tails that are wall-collectable. Figures 4(c) and 4(d) show similar depletions of the VDF tails at points $Q_1$ and $Q_2$. In plot 4(c) the peak on the $s1$-VDF (blue line) corresponds to the electrons just emitted from $W_1$, which have acquired an electric potential energy $e\Delta\phi_{W_1Q_1} = 11.43$eV when crossing the sheath. An equivalent explanation applies to the peak of the $s2$-VDF (red line) in plot 4(d), with an energy $e\Delta\phi_{W_2Q_2} = 12.74$eV.

Beyond these peaks, the shape of the VDFs for secondary electrons at different locations is the consequence of their possible destinies. The most energetic ones are recollected after a single or double radial journey. The rest of them bounce radially, until collisions make them preferentially to 'thermalize' into the primary population. The SEE yield and the amounts of wall-recollection and thermalization determine the density and other macroscopic properties of secondary electrons. Table 2 provides detailed data on these processes: 60% and 63% of $s1$ and $s2$ electrons, respectively, are thermalized into $p$ electrons due to electron-neutral or large angle Coulomb collisions, while the remaining fractions are re-collected at the walls.

Table 2 also provides the currents of the different electron species to and from the walls. Most of the current to the walls comes from the $p$-population, which has a much larger density, as illustrated in Figure 5(a). The most prominent result is that large asymmetries are found between walls in, first, the current exchanged at each of them, with a ratio of $|j_{e,2+}|/|j_{e,1-}| \simeq 1.59$, and, second, the average true-secondary yields, defined as

$$< \delta_{TS,1} >= \frac{|j_{s1,1+}|}{|j_{e,1-}|} \approx 0.15, \qquad < \delta_{TS,2} >= \frac{|j_{s2,2-}|}{|j_{e,2+}|} \approx 0.29. \tag{23}$$

for each wall. Here and in Table 2: subscripts 1 and 2 refer to each wall, and + and - to the direction of the radial velocity at the wall. Since the two wall materials are the same, the difference in the effective SEE yields must be due to a difference in the mean impacting energy per particle, $E_w$. This can be obtained dividing a net energy flux to a wall by the corresponding particle flux. Table 2 shows, indeed, that $E_{wp,1} = 8.5$eV and

$E_{wp,2} = 15.7$eV. In fact, these values are not far from twice the electron temperature, the value obtained for fluxes of a Maxwellian distribution.

Figure 5 plots steady-state spatial profiles for main macroscopic magnitudes. The discussion here will be focused on the plasma bulk, since behaviors of plasma magnitudes inside the steepened sheaths (such as the behavior of $T_e$) are generally not detailed in the conventional two scale sheath analysis. Figure 5(a) plots the density profiles of the different electron populations, confirming the much lower densities of secondary electrons. In addition, a large asymmetry between $s1$ and $s2$ densities is observed. The lower $s1$-density is partially caused by the lower SEE yield from $W_1$.

Figure 5(b) plots the macroscopic radial velocity $u_r$ for the three electron populations. Primary electrons behave as usual with inward and outward fluxes from around the channel mid-line $M$. The velocity increase inside the sheaths is just the consequence of the decreasing density there. Indeed, the same behavior is observed in the radial velocity of ions, Fig. 5(c), where $M_{ri} = u_{ri}/\sqrt{T_e/m_i}$ is the radial Mach number. Observe that the sheath edges were placed at the ion sonic points.

Back into Fig. 5(b), $s1$-electrons present a net outwards radial velocity, indicating that their outwards flow is slightly larger than the inwards one, due to a larger recollection at $W_2$. The opposite situation happens to $s2$-electrons. Notice that these radial velocities are just small drifts in the VDFs of the three populations: for instance, the energy corresponding to $u_r = 10^5$m/s is $\sim$0.03 eV. The similar negative slope of $du_r/dr$ for $s1$ and $s2$ electrons is likely due to the net macroscopic effect of the magnetic mirror and the $E \times B$ contributions.

Figure 5(d) plots the macroscopic axial velocities $u_z$ of the three electron populations. These velocities are practically zero except for the oscillations shown in SEE electrons which correspond to the net axial residual of their gyromotion, also known as near wall conductivity [13]. Although not shown here, ions present an average macroscopic velocity approximately equal to that assigned individually to their macroparticles when created. Very importantly, the simulations confirm that there are not secular effects on the axial flow of all populations and therefore no need of performing particle refreshing, as in the previous version of the code. (Nonetheless, collisional effects in much longer simulations should yield a non-zero electron axial velocity of the order of $u_{\theta e}$ divided by the Hall parameter.)

Figure 3(b) showed the mean temperatures of the three electron species. Now, Figs. 5(e) and 5(f), plot their radial (i.e. $B$-parallel) and perpendicular temperatures, unveiling a significant anisotropy. For the three populations, it is found $T_\theta \approx T_z \approx T_\perp$ and the anisotropy is the combined consequence of the electron magnetization and depletion at walls. Interestingly and due to their very different dynamics, $T_r/T_\perp$ is lower than 1 for primary electrons and larger than 1 for secondary electrons. For instance, at point $M$ one has $T_{rp,M}/T_{\perp p,M} \simeq 0.64$, $T_{rs1,M}/T_{\perp s1,M} \simeq 4.35$, and $T_{rs2,M}/T_{\perp s2,M} \simeq 2.08$. The temperature behavior of primary electrons is a direct consequence of the partial depletion of the radial VDF tail. The trend $T_r/T_\perp > 1$ for secondary electrons would be due to their preferential radial bouncing, further enhanced by the fact that when they collide strongly they are moved to the primary population.

Because of the very low density of secondary electrons, the radial potential profile of Fig. 5(a), is shaped almost exclusively by the $p$-population. Indeed, the macroscopic radial equilibrium for $p$ electrons, taking into account magnetic mirror effects (i.e. temperature anisotropy) and the radial centrifugal force (coming from the $E \times B$ drift) reads

$$e\frac{d\phi}{dr} - T_{rp}\frac{d\ln n_p}{dr} - \frac{dT_{rp}}{dr} + \frac{T_{\perp p} - T_{rp}}{r} + \frac{m_e u_{\theta p}^2}{r} = F_{r,col}, \tag{24}$$

where: $d\ln B/dr = -1/r$ was applied in the last-but-one term of the left side, and $F_{r,col}$ groups all collisional effects. The dominant terms in this balance are of order $\sim T_{rpM}/e(r_2 - r_1) \approx 300$V/m. Figure 6 plots the collisional contribution, showing that it is negligible, as expected (the large oscillations of the curve are due mainly to inaccuracies related to computing spatial derivatives from noisy PIC profiles). Neglecting collisions, the integration of the above equation yields

$$(e\phi - e\phi_M) - T_{rpM}\ln\frac{n_p}{n_{pM}} = (T_{rp} - T_{rpM}) + \int_{r_M}^{r} dr\left[(T_{rp} - T_{rpM})\frac{d\ln n_p}{dr} - \frac{T_{\perp p} - T_{rp}}{r} - \frac{m_e u_{\theta p}^2}{r}\right]. \tag{25}$$

Here, the left side groups the terms of the Boltzmann-Maxwell relation, and the right-side groups all terms (non-uniform radial temperature, temperature anisotropy, and centrifugal force) affecting their fulfillment. Figure 6(b) shows, first, that the whole radial equilibrium of Eqs. (24) and (25) is excellently satisfied, and, second, the simplification of Eq. (25)to just the Boltzmann relation yields error of up to a 30%. In the present simulation, the three terms affecting that relation are of the same order.

The potential fall in a sheath is closely related to the electron currents to and from the walls. In particular, the lower is the primary electron current because of its VDF tail depletion, the lower is the required potential fall to fulfill the zero electric current condition. Ahedo and dePablo 8 analyzed this problem analytically assuming a functional form of the $p$-VDF which fits well with the present results. They modelled the partial depletion with

a replenishment (thermalization) parameter $\sigma_t$ (not to be mistaken this symbol with a surface charge), which, in the end, measured the ratio between the actual potential fall and the one corresponding to a non-depleted Maxwellian population. For instance, for the inner wall $W_1$ it would be

$$\sigma_{t,1} = \frac{|j_{pW_1}|}{j_{ther,1}} \qquad \text{with} \qquad j_{ther,1} = en_{pQ_1} \exp\left(-e\frac{\phi_{W_1Q_1}}{T_{pQ_1}}\right)\sqrt{\frac{T_{pQ_1}}{2\pi m_e}}, \tag{26}$$

and a similar definition for the outer wall. In our simulation, the $p$-tail replenishment ratios are rather small, $\sigma_{t,1} \simeq 0.04$ and $\sigma_{t,2} \simeq 0.05$, which seems reasonable with the weak electron collisionality. If instead of the total temperature $T_p$, the radial temperature $T_{rp}$ were used in the definition of $j_{ther}$, it would still be $\sigma_{t,1} \simeq 0.15$ and $\sigma_{t,2} \simeq 0.19$.

A final point to comment is that, in the present ionization-controlled model with no axial (i.e. external) injection of particles along the simulation, the mean steady-state electron temperature is totally intrinsic to the model and its parameters. Indeed, simulations started with different values of $T_{e0}$ between 1 and 20 eV lead to the same final temperatures shown here. This final temperature comes out from the energy balance

$$P_{sinks} = P_{sources}, \qquad P_{sinks} \simeq P_{inel} + P_{wall,t}, \qquad P_{sources} \simeq P_{elec} + P_{wall,f}, \tag{27}$$

where: $P_{inel}$ the losses due to inelastic processes (ionization and excitation), $P_{wall,t}$ the losses due to electron collection at the walls, $P_{wall,f}$ the gains due to electron emission at the walls, and $P_{elec}$ the energy transmitted to electrons by the electric field. The values are in Table 2: $P_{wall,f}$ is negligible and $P_{inel}$ and $P_{wall,t}$ are of the same order. In the opposite case of an axially-controlled radial discharge, i.e. with $S_{axial,j} \gg S_{ioniz}$ in Eq. (1), the mean $T_e$ would be dependent mainly of the temperature of the macro-electrons continuously injected through $S_{axial,j}$. Therefore, while the temperature anisotropy of the primary population and the temperatures of the secondary populations are relevant results of a 1Dr model, the mean value of $T_e$ is partially arbitrary. Indeed, in a Hall thruster discharge, $T_e$ is determined basically by the axial dynamics, through the discharge voltage and related the Joule heating (plus the effects of ionization and wall cooling).

# 5 Conclusions

The annular model and related PIC/MCC code of given axial section of the acceleration region of a HET was built on a previous one by Taccogna. The main numerical improvements and conclusions are the following. First, in an ionization-controlled discharge we cannot fix both the mean neutral density and the mean plasma density. Second, to fix the plasma density and to adjust in time the background neutral density is a preferable method in terms of optimizing the PIC implementation. Third, secular growth of ion axial energy and subsequent refreshing of macro-ions is avoided. And fourth, a time-extended volumetric weighting algorithm is implemented, which improves very substantially the weighting of macroscopic magnitudes of minor species (here the true-secondary electrons), while not affecting the major species (here the primary electrons and the ions).

On the physical side the main contributions are the following. First, because of the weak collisionality (dominated by elastic electron-neutral collisions), the primary VDF presents an important depletion of high-radial-energy tails, leading to a radial-to-perpendicular temperature anisotropy ratio of about 2/3. Second, true-secondary electrons are partially thermalized into primary electrons and partially recollected by the walls, in a proportion about 60%-40%. Their resulting density is very low and thus has no effect in shaping the electric potential profile. Besides, they keep a small radial drift velocity and a temperature anisotropy with a radial-to-perpendicular temperature ratio larger than one. Third, there is a significant asymmetry in the plasma structure, with differences of a factor about 2 in the electron currents to and from the walls and in the mean wall-impact energies. Fourth, the electric potential profile in the quasineutral plasma bulk is determined from a radial equilibrium which goes beyond the usual Maxwell-Boltzmann relation on primary electrons (secondary electrons) and incorporates effects of (i) non-uniformities of the radial temperature, (ii) magnetic mirror, and (iii) the centrifugal force. The magnetic mirror effect is indeed a combination of temperature anisotropy and cylindrical divergence. The presence and relevance of the centrifugal force is worth to stand out since it is generally disregarded in macroscopic models by invoking the zero electron-inertia limit. Fifth, the replenishment ratio of the high radial-energy tail of primary electrons has been estimated in a few percent and this parameter can also be very useful in macroscopic two-scale models to model the sheath potential fall.

Further work will have to carry out a parametric investigation on the trends identified here, in an attempt to derive of scaling laws among them. These laws provide relevant insight on the discharge behavior and can be implemented in macroscopic models of electrons, such as the one used in 2D hybrid HET codes. Particular interest will have to increase the axial electric field in order to reach electron azimuthal velocities above the thermal velocity and analyze the reported transition from a stationary solution to an instability saturated one. In a different direction of research, the plasma response to a non-purely radial magnetic field should have important consequences on the electron VDFs.

# 6 Acknowledgments

The work at UC3M was supported by the CHEOPS project, funded by the European Union's Horizon 2020 Research and Innovation Programme, under Grant Agreement 730135. Additional support came from the Spain´s National Research and Development Plan (Project ESP2016-75887). F. T. was supported by the ApuliaSpace Project (grant PON03PE_00067_6).

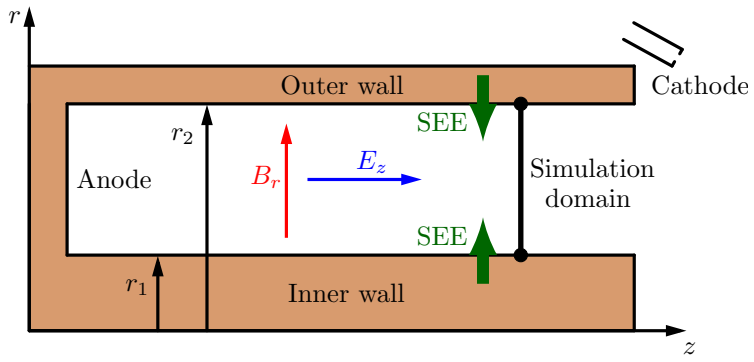


Figure 1: Sketch of a HET. The simualation domain is black line cross-section.

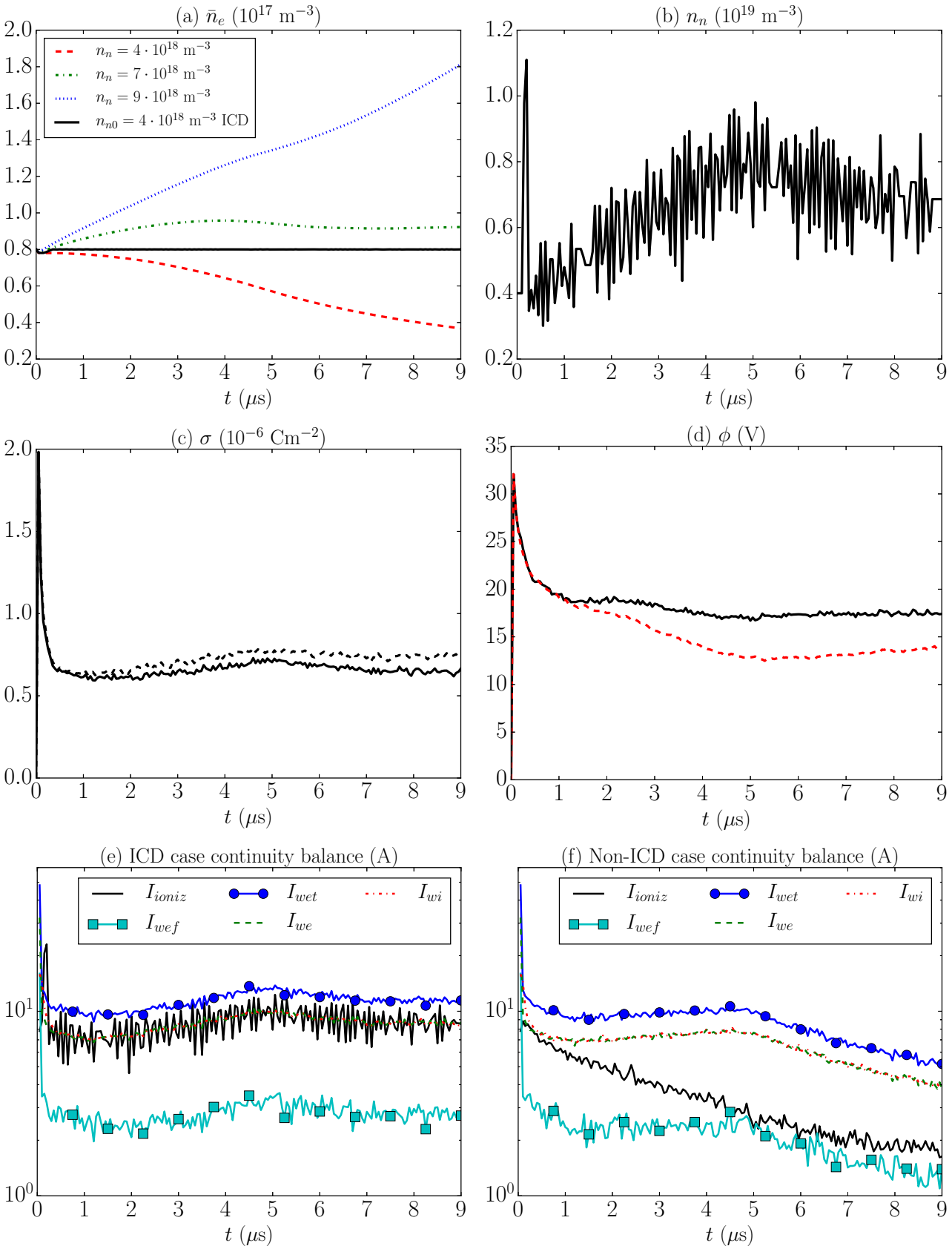


Figure 2: Time evolution of: (a) the average electron density in the simulation domain for non-ICD (dashed) and ICD (solid) cases; (b) the background neutral density in the ICD case of previous plot; (c) surface charge densities at the inner (black solid) and outer (black dashed) walls in the ICD case; and (d) the electric potential at the central point $M$ in the ICD (black solid) and non-ICD cases (red dashed). Time evolution of the different electron sources and sinks on the current continuity balance of Eq. (15) for the (e) ICD and (f) non-ICD cases. All plots represent time-averaged magnitudes over $N_k = 10^4$ timesteps.

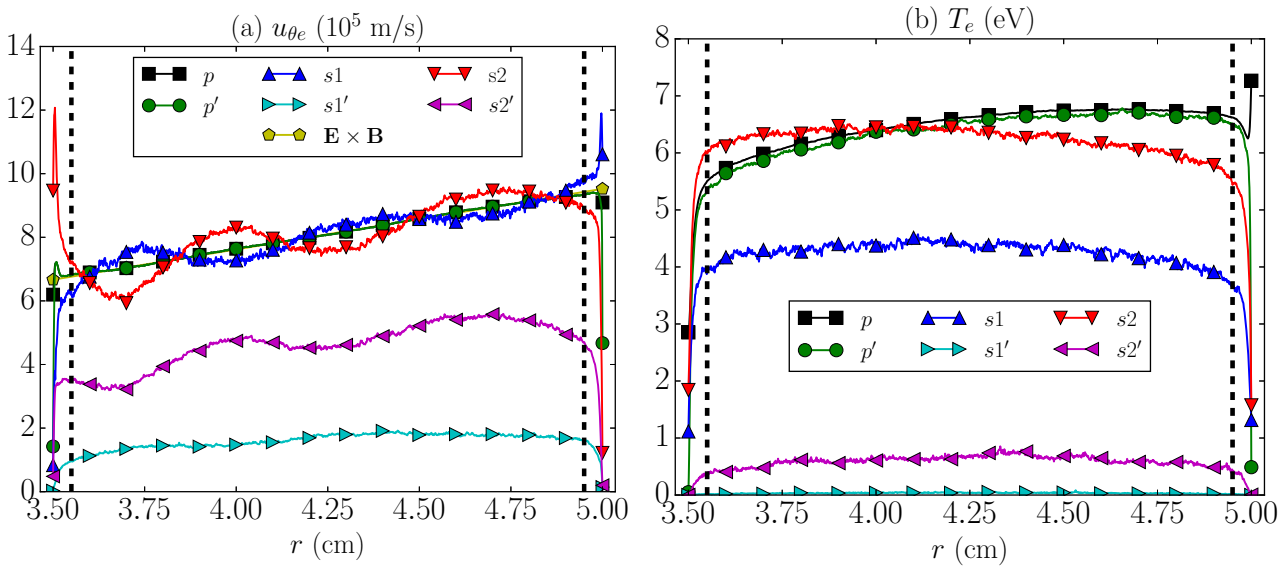


Figure 3: Steady-state radial profiles of (a) azimuthal fluid velocities and (b) mean temperatures of the different electron populations. Curves without (with, resp.) a prime correspond to extended (standard, resp.) volumetric weighting. Plot (a) also depicts the $E \times B$ velocity drift for comparison. Steady-state values have been averaged over the last $N_k = 2 \cdot 10^5$ timesteps. In both plots the vertical dashed lines represent the approximate inner and outer sheath edges.

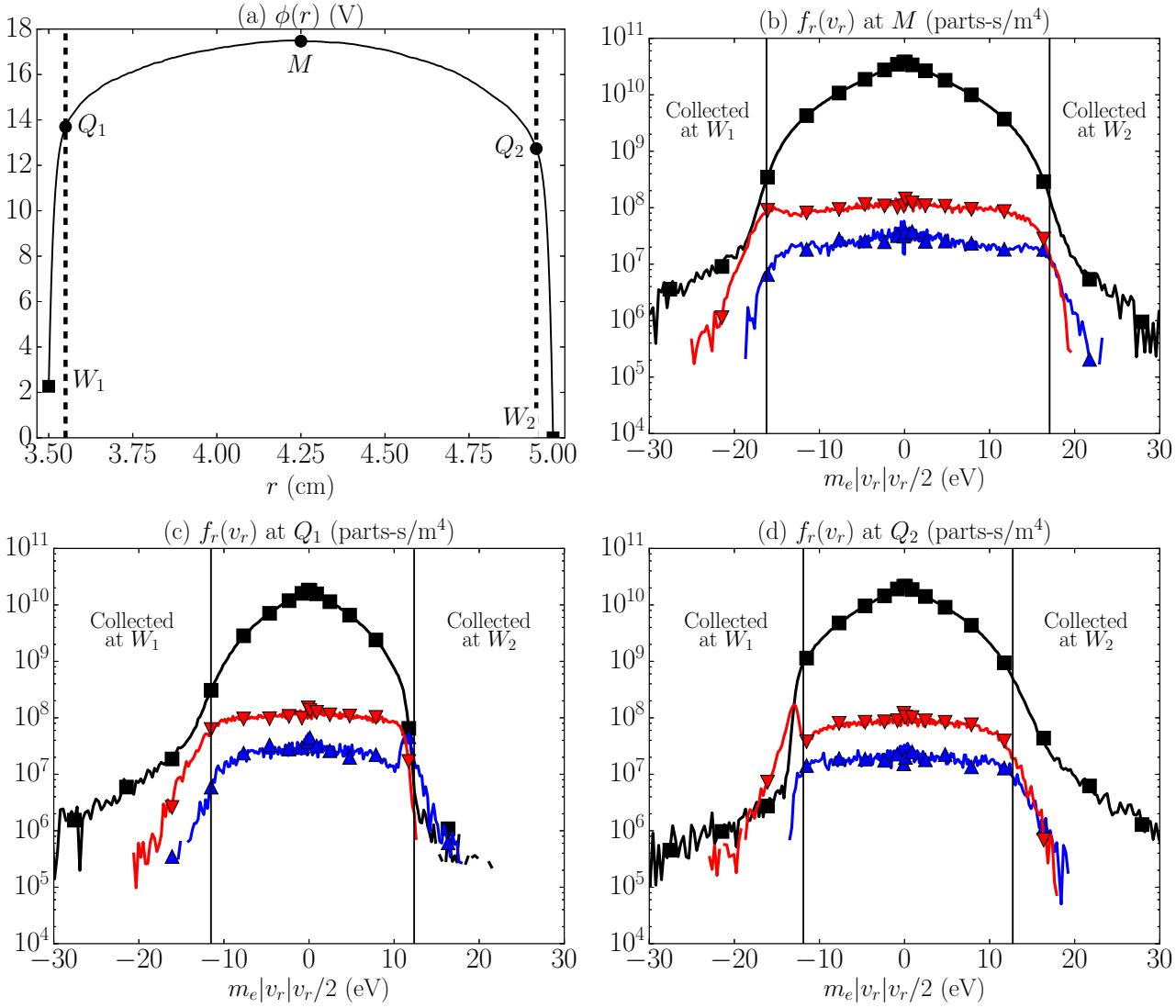


Figure 4: (a) Time-averaged (over last micro-second of simulation time) radial profile of the electric potential. Points $M$, $Q_1$, $Q_2$, $W_1$, $W_2$ correspond to channel midradius, sheath edges, and walls. (b)-(d) Radial velocity distribution function at nodes $M$, $Q_1$, and $Q_2$. Black, blue and red lines with square, up and down triangles correspond to the $p$, $s1$ and $s2$ populations, respectively. The VDFs have been accumulated over the last micro-second of simulation time.

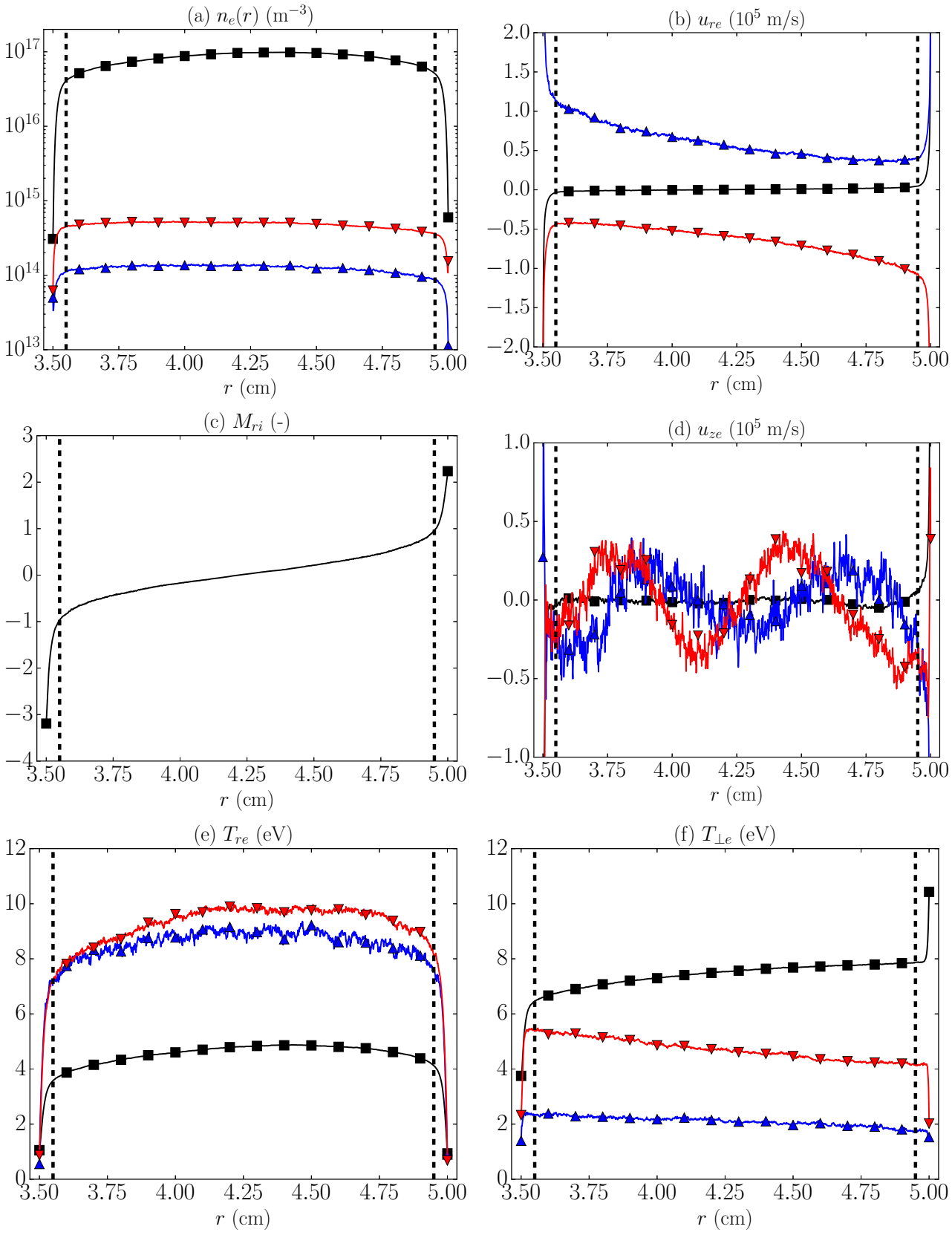


Figure 5: Steady-state radial profiles of macroscopic magnitudes for the different electron species and ions: (a) electron particle density, (b) electron radial velocity, (c) ion radial velocity, (d) electron axial velocity, (e) radial electron temperature, and (f) perpendicular electron temperature. Black, blue and red lines with square, up and down triangles correspond to $p$, $s1$ and $s2$ electron populations, respectively. Dashed vertical lines mark approximate sheath edges. Curves are computed using the EVW scheme with the last $N_k = 2 \cdot 10^5$ timesteps.

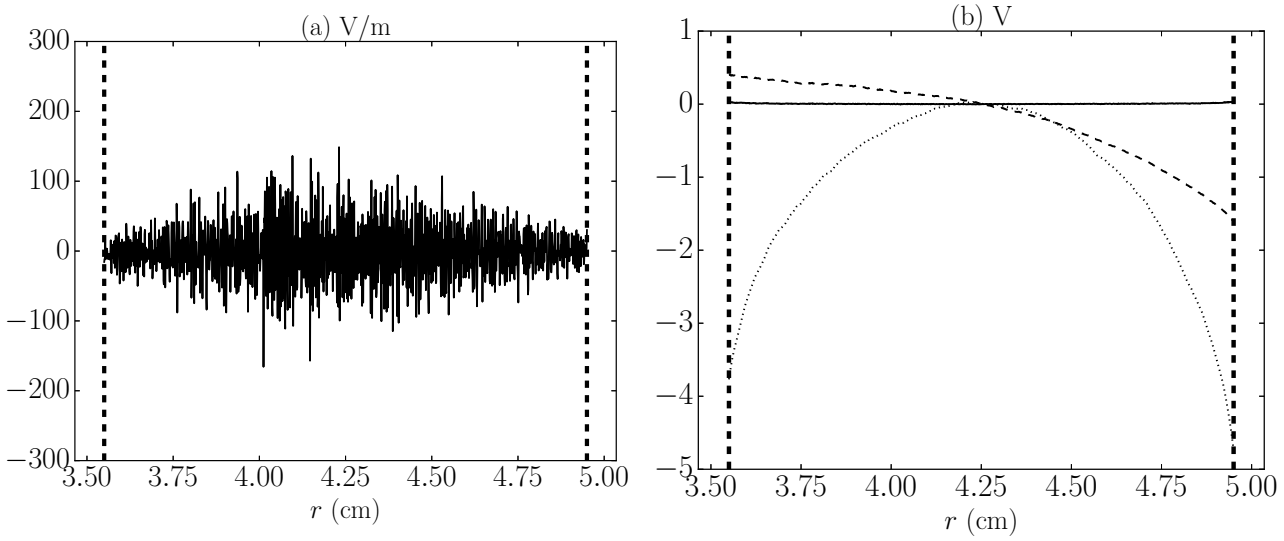


Figure 6: (a) Contribution of collisional and other minor effects to the local radial momentum balance of electrons, Eq. (24). (b) (solid line) Fulfilment of the integrated radial momentum balance of electrons, Eq. (25); (dashed line) Maxwell-Boltzmann relation; (dotted line) electric potential profile reference to $\phi_M$. Dashed vertical lines mark approximate sheath edges.

# References


[1] E. Ahedo. Plasmas for space propulsion. *Plasma Phys. Control. Fusion*, 53(12):124037, 2011.

[2] D. M. Goebel and I. Katz. *Fundamentals of electric propulsion: Ion and Hall thrusters*. Willey, New York, 2008.

[3] R. G. Jahn. *Physics of electric propulsion*. McGraw-Hill, New York, 1968. (reprinted by Dover).

[4] S. Barral, Z. Peradzynski, K. Makowski, and M. Dudeck. An alternative theory of transit-time oscillations in Hall thrusters. In *Proc. 28th International Electric Propulsion Conference, Toulouse, France*, IEPC 03-335, 2003.

[5] E. Ahedo and F.I. Parra. Model of radial plasma-wall interactions in a Hall thruster. In *Proc. 38th Joint Propulsion Conference, Indianapolis, IN*, AIAA 2002-4106, 2002.

[6] E. Ahedo, J. M. Gallardo, and M. Martínez-Sánchez. Effects of the radial-plasma wall interaction on the axial Hall thruster discharge. *Phys. Plasmas*, 10(8):3397–3409, 2003.

[7] E. Ahedo and F. I. Parra. Partial trapping of secondary electron emission in a Hall thruster plasma. *Physics of Plasmas*, 12(7):073503, 2005.

[8] E. Ahedo and V. de Pablo. Combined effects of electron partial thermalization and secondary emission in Hall thruster discharges. *Physics of Plasmas*, 14:083501, 2007.

[9] D. Sydorenko, A. Smolyakov, I. Kaganovich, and Y. Raitses. Modification of electron velocity distribution in bounded plasmas by secondary electron emission. *Plasma Science, IEEE Transactions on*, 34(3):815–824, 2006.

[10] I. D. Kaganovich, Y. Raitses, D. Sydorenko, and A. Smolyakov. Kinetic effects in a hall thruster discharge. *Phys. Plasmas*, 14(5):057104, 2007.

[11] C. K. Birdsall. Particle-in-Cell charged particle simulations, plus Monte Carlo collisions with neutral atoms, PIC-MCC. *Trans. Plasma Sci.*, 19(2):65–85, 1991.

[12] R. W. Hockney and J. W. Eastwood. *Computer simulations using particles*. Adam Hilger, Bristol and New York, 1988.

[13] A.I. Bugrova, A. I. Morozov, and V. K. Kharchevnikov. Experimental studies of near wall conductivity. *Fizika Plazmy*, 16(12):1469–1481, 1990.

[14] H. Wang, M. Campanell, I. Kaganovich, and G. Cai. Effect of asymmetric secondary emission in bounded low-collisional e× b plasma on sheath and plasma properties. *Journal of Physics D: Applied Physics*, 47(40):405204, 2014.

[15] F. Taccogna, S. Longo, M. Capitelli, and R. Schneider. Particle-in-cell simulation of stationary plasma thruster. *Contributions to Plasma Physics*, 47(8-9):635–656, 2007.

[16] F. Taccogna, S. Longo, M. Capitelli, and R. Schneider. Surface-driven asymmetry and instability in the acceleration region of a Hall thruster. *Contrib. Plasma Phys.*, 48(4):1–12, 2008.

[17] F. Taccogna, R. Schneider, S. Longo, and M. Capitelli. Kinetic simulations of a plasma thruster. *Plasma Sources Sci. Technol.*, 17(2):024003, 2008.

[18] M. A. Furman and M. T. F. Pivi. Probabilistic model for the simulation of secondary electron emission. *Phys. Rev ST Accel. Beams*, 5(12):124404, 2002.

[19] K. Nanbu. Probability theory of electron-molecule, ion-molecule, molecule-molecule, and Coulomb collisions for particle modeling of materials processing plasmas and gases. *Trans. Plasma Sci.*, 28(3):971–990, 2000.

[20] K. Nanbu. Simple method to determine collisional event in Monte Carlo simulation of electron-molecule collision. *Jpn. J. Appl. Phys.*, 33(8):4752–4753, 2000.

[21] M. Surendra, D. B. Graves, and I. J. Morey. Electron heating in low-pressure rf glow discharges. *Appl. Phys. Lett.*, 56(11):1022–1024, 1990.

[22] K. Nanbu. Theory of cumulative small-angle collisions in plasmas. *Phys. Rev. E*, 55(4):4642–4652, 1997.

[23] K. Nanbu and S. Yonemura. Weighted particles in Coulomb collision simulations based on the theory of a cumulative scattering angle. *J. Comput. Phys.*, 145:639–654, 1998.

[24] A. V. Bobylev and K. Nanbu. Theory of collision algorithms for gases and plasmas based on the Boltzmann equation and the Landau-Fokker-Plack equation. *Phys. Rev. E*, 61(4):4576–4586, 2000.

[25] C. Wang, T. Lin, R. Caflisch, B. I. Cohen, and A. M. Dimits. Particle simulation of Coulomb collisions: comparing the methods of Takizuka & Abe and Nanbu. *J. Comput. Phys.*, 227:4308–4329, 2008.

[26] C. K. Birdsall and A. B. Langdon. *Plasma physics via computer simulation.* Adam Hilger, Bristol, Philadelphia and New York, 1991.

[27] J. P. Verboncoeur. Symmetric spline weighting for charge and current density in particle simulation. *Journal of Computational Physics*, 174:421–427, 2001.

[28] R. Santos, E. Ahedo, and R. Santos. Implementation of the kinetic Bohm condition in a Hall thruster hybrid code. In *45th AIAA/ASME/SAE/ASEE Joint Propulsion Conference & Exhibit*, page 4913, 2009.

[29] E. Ahedo, R. Santos, and F. I. Parra. Fulfillment of the kinetic Bohm criterion in a quasineutral particle-in-cell model. *Physics of Plasmas*, 17(7):073507, 2010.

[30] W. H. Press, S. A. Teukolsky, W. T. Vetterling, and B. P. Flannery. *Numerical recipes in Fortran 77: the art of scientific computing.* Cambridge University Press, New York, 2001. Available online: http://numerical.recipes/.

[31] J. J. Szabo, Jr. *Fully kinetic numerical modeling of a plasma thruster.* PhD thesis, Aeronautics and Astronautics Dept., Massachuchusetts Institute of Technology, Boston, February 2001.